Original Article

Institution of MECHANICAL ENGINEERS
Journal of AEROSPACE ENGINEERING

Proc IMechE Part G:
J Aerospace Engineering
2016, Vol. 230(8) 1397–1408

DOI: 10.1177/0954410015611151
uk.sagepub.com/jaero
SAGE

The design and performance evaluation of axial ventilator with honeycomb in the turbofan engine lubrication system

Zhao Jingyu, Liu Zhenxia and Ren Guozhe

Abstract

Numerical simulations have been carried out to investigate the performance of the axial ventilator equipped with honeycomb structure. The oil /air two-way coupling model based on the Realizable k–ε turbulence model and the droplet impact model are proposed. Based on verifying the rationality of numerical model, characteristics of flow resistance and oil–gas separation efficiency are calculated and analyzed. The results show that the axial ventilator with honeycomb has favorable separation efficiency, which is estimated as 99.6% for the oil droplet diameter of 5 μm. The honeycomb structure has little effect on flow resistance, but plays a major role in the oil–gas separation of axial ventilator, where the contribution to the oil separation accounts for 80% at least. Besides, the increase of rotation Reynolds number enhances the centrifugal force, resulting in the increase of separation efficiency, while the increase of nondimensional mass flow rate and environmental temperature reduce the residence time of oil droplets in the axial ventilator mainly, resulting in the decreasing of separation efficiency.

Keywords

Axial ventilator, honeycomb structure, oil droplet–wall interaction, flow resistance, separation efficiency

Date received: 23 April 2015; accepted: 15 September 2015

Introduction

In the aero-engine, axial ventilator is usually designed as a whole with the main shaft, which has been successfully applied to variety types of engines, such as CFM56, F110, etc.[1] The design of axial ventilator can realize oil–gas separation, thus reducing the oil consumption of lubricating oil system. Furthermore, the integrated design of ventilator and aero-engine main shaft can simplify the structure of engine, such as the external vent pipes and supported plates, and even dispense with traditional centrifugal ventilator, which will reduce the weight of aero-engine, and be beneficial to enhancing the overall performance of aero-engine.

The internal flow field of axial ventilator is relatively complex with the characteristics of high rotation speed, strong turbulence and two-phase separation, and has a direct effect on the oil separation. Therefore, the oil–gas two-phase flow calculation of internal flow field in the axial ventilator is of the great significance to the oil–gas separation research, and involves two main aspects to be specific: the oil–gas two-phase movement and the oil–wall interaction.

In the aspect of the oil and gas two-phase movement, Euler–Lagrange approach is generally utilized to calculate the movement of air and droplets in the oil–air separators. For instance, Elsayed et al.[2] and Eastwick et al.[3] numerically carried out the internal flow field for the oil–gas separators using the discrete phase model (DPM). And Xu et al.[4] studied the two-phase flow field of a certain axis ventilator, and simulated the turbulent velocity pulsation effects on oil droplets trajectories using DRW model. As for the coupled calculation between the air and oil droplets, there are two main methods: one-way coupling and two-way coupling. The difference between them is whether the influence of the droplet on air movement is considered or not. Farrall[5] earlier studied the oil–gas flows in the bearing chamber using one-way coupling method. However, experiment studies indicated that the oil–gas coupling existed under some harsh aero-engine environment. Bachalo et al.[6] measured the effect of the flow vortex on oil droplets with a diameter range of 10–50 μm by using Doppler analyzer, and results showed the strong coupling

School of Power and Energy, Northwestern Polytechnical University, Xi'an, PR China

Corresponding author:
Zhao Jingyu, School of Power and Energy, Northwestern Polytechnical University, No.1, Dongxiang Road, Chang'an District, Xi'an, Shaanxi, 710129, PR China.
Email: jingyu_nwpu@126.com

relationship between oil and gas two-phase flow. Gorse et al.[7] conducted studies for the oil droplets movement under high ambient temperature, and results revealed that the droplets motion and evaporation had a certain effect on air velocity and the distribution of turbulent kinetic energy. Recently, Liu et al.[8,9] established the oil /air two-way coupling mathematical model for the internal flow field of bearing chamber, numerical results showed that the effect of oil droplets on the airfield should not be ignored.

In the aspect of the oil–wall interaction, the present studies mainly focus on the establishment of the impingement criteria. Mundo et al.[10] and Cossali et al.[11] studied the single droplet impingement characteristics on the liquid film surface, and proposed criteria of splash, spread, etc. by high-speed photography. Bai et al.[12] established impingement calculation models of various phenomena, which contained adhesion, rebound, spread, and splash. In addition, Stanton et al.[13] analyzed the interaction between droplets and wall, and put forward the interaction rule of oil droplets collision, in which selected impact energy and the wall temperature as the judgment criterion.

Flow resistance and oil–gas separation efficiency are important indexes to measure the performance of axial ventilator. In recent years, some relevant institutions constantly design and improve the structure of axial ventilator, so that it could have better separation efficiency and appropriate flow resistance characteristics, and one of means is the application of the new structure as the filter element in the axial ventilator, such as metal foam, honeycomb, etc. For instance, Willenborg et al.[14] added the metal foam structure into the aero-engine ventilation, and carried out the experiments on the performance of ventilator.

The aim of the present work is to figure out the performance of newly designed axial ventilator with honeycomb structure. Considering the similar internal flow field characteristic to the bearing chamber and high temperature environment (near turbine) in the axial ventilator, the oil /air two-way coupling model and the droplet impaction model are established. ANSYS-Fluent software is utilized in the numerical computation, and the characteristics of flow resistance and oil–gas separation efficiency under different conditions are achieved. Besides, the coincidence with experimental data proves that the calculation analysis model here is reasonable and effective.

Configuration of axial ventilator with honeycomb

Figure 1 shows the cross-sectional view of axial ventilator setup with honeycomb, which mainly consists of the honeycomb structure, Ring-cavity A, Hole A (Six holes), Ring-cavity B, Hole B (Six holes) and the channel of central axis according to the sequence of oil–gas flow through the ventilator. Hole A and Hole B are both radial holes with the circular distribution uniformly, and stagger each other with the angle of 30°. In the experiment, the whole ventilator is placed in a large pressure-stabilizing cavity, and this cavity provides stable pressure and oil–gas environment. At work, the entire ventilator runs with high-speed rotary motion, and the mixture of oil and gas enters the axial ventilator from the pressure-stabilizing cavity. The oil is separated by wall structures of honeycomb,

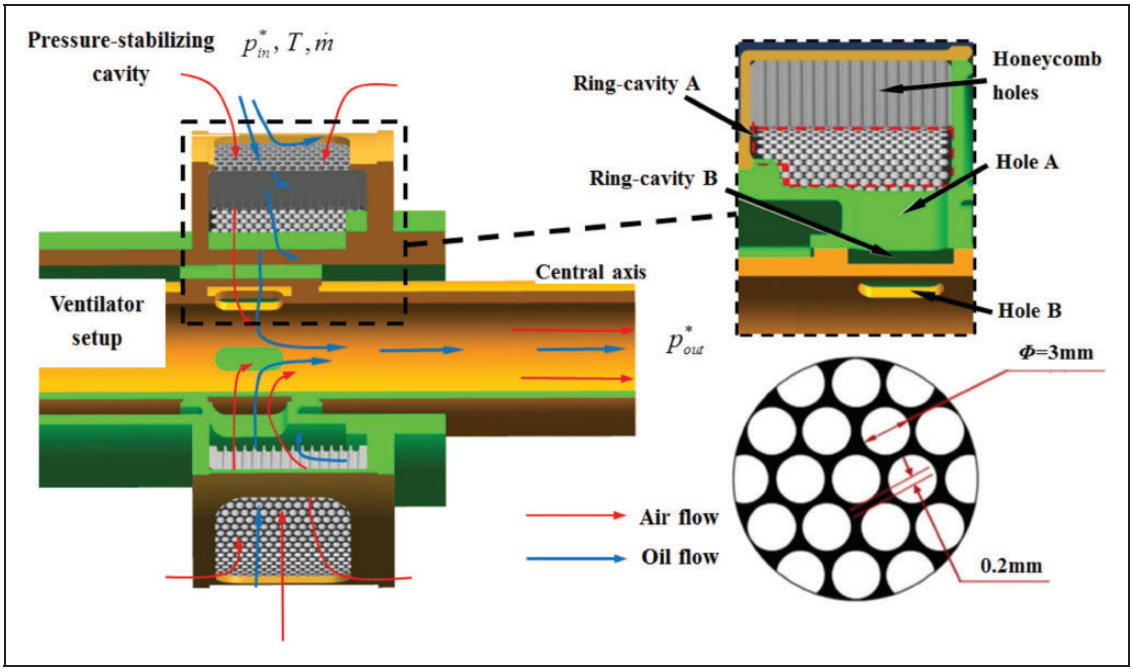

Figure 1. Flow path structure of axial ventilator setup with honeycomb.

ring-cavities, and radial holes in turn. Finally, the non-separated oil and air leave from the channel of central axis. The honeycomb consists of a large number of radial holes, and is the main oil–gas separation structure. The diameter of honeycomb hole is 3 mm, and the spacing is 0.2 mm, as shown in Figure 1.

Experiment study is completed on the lubrication system test platform, which mainly consists of the axial ventilator test rig, oil feed system, air feed system, measurement system, power system, and oil recycling system. Airflow, provided by compressed gas-tank, is controlled by the gas flow meter, and enters the ventilator from the pressure-stabilizing cavity with the oil. In the experiment, the wall separated oil and the outlet oil of ventilator (nonseparated oil) are collected respectively, and then the mass of oil is measured by electronic balance with the accuracy of 10^{-5}. Moreover, the inlet and outlet pressure data, with the accuracy of 0.5%, are measured in the pressure-stabilizing cavity and the exit of central axis respectively. Considering the factors of systematic error, working conditions etc., the relative uncertainty for pressure data is less than 4.5%, and the relative uncertainty for oil–gas separation is less than 0.5%.

Numerical model and methodology

In this paper, the mass ratio of oil and gas is 2.5%. Considering the densities of air and oil, the volume fraction of oil flow within the airflow is less than 10^{-4}, so Euler–Lagrange approach is utilized to calculate the movement of air and droplets in the axis ventilator.

Two-way coupling flow

The two-way coupling calculation[15] of the airfield and oil droplet motion is adopted. For the airflow, control equations are established in Euler system, and the interaction between the oil droplet and air is represented by the source term. The Reynolds-averaged Navier–Stokes equations of the airflow can be written as follows:

Continuity equation

$$\frac{\partial}{\partial x_i}\left(\rho \bar{U}_i\right) = S_m \tag{1}$$

where ρ and U stand for the gas density and velocity, S_m is the additional source term for the continuity equation, and oil evaporation could change it in the oil–gas two-phase flow of ventilator. Here, S_m can be expressed as

$$S_m = \frac{1}{V}\sum \dot{m}_d \tag{2}$$

Momentum equation

$$\frac{\partial}{\partial x_j}(\rho \overline{U_i U_j}) = -\frac{\partial p}{\partial x_i} + \frac{\partial \tau_{ij}}{x_j} + \rho g_i + S_{Ui} \tag{3}$$

where τ is the shear stress, S_U is the additional source term for the momentum equation, and the momentum influence between the oil and air consists of two parts: one is the drag force from the droplet–air interaction, which is the momentum exchange caused by droplet motion, named as $S_{Ui,d}$. It can be expressed as

$$S_{Ui,d} = \frac{1}{V}\sum\left[-m_d\left(\frac{\mathrm{d}U_{di}}{\mathrm{d}t} - g_i\right)\right] \tag{4}$$

The other part is the momentum term caused by evaporation, which is the momentum exchange caused by droplet steam, named as $S_{Ui,m}$. Based on the assumption that the oil droplet and its steam have the same velocity, it can be expressed as

$$S_{Ui,m} = S_m \cdot U_{di} \tag{5}$$

Energy equation

$$\frac{\partial}{\partial x_i}\left(\rho e \bar{U}_i\right) = -p\frac{\partial U_i}{\partial x_i} + \tau_{ij}\frac{\partial U_i}{\partial x_j} + \frac{\partial}{\partial x_i}\left(k\frac{\partial \bar{T}}{\partial x_i}\right) + S_E \tag{6}$$

where e, k, and T respectively stand for the internal energy, thermal conductivity, and mean temperature defined with respect to a reference temperature T_{ref}. S_E is the additional energy source term for equation, and can be divided in two parts: $S_{E,d}$ represents the heat captured by the droplet for its heating and for evaporation mass of liquid per unit time, and $S_{E,m}$ represents the heat which is released by the droplet into the fluid, it can be expressed as

$$S_{E,d} = \frac{1}{V}\sum\left(-4\pi r_d^2 q_s\right) \tag{7}$$

$$S_{E,m} = \frac{1}{V}\sum\left[\dot{m}_d C_{vap}\left(T_s - T_{ref}\right)\right] \tag{8}$$

where q_s is the heat rate on droplet surface, and C_{vap} is the evaporation specific heat.

Oil droplet motion

The trajectory of oil droplets can be solved through a Lagrange particle tracking method. In this paper, the droplets are rigid spheres, and the oil droplets neither coalesce nor break up. Considering the size of oil droplets, density difference between oil and gas, oil droplets velocity, environmental temperature, etc., the viscosity drag force $\boldsymbol{F_D}$, centrifugal force $\boldsymbol{F_R}$, Brown force $\boldsymbol{F_B}$, Saffman's lift force $\boldsymbol{F_S}$, and gravity

are taken into account through force analysis.[16,17] The equation of particle motion can be expressed as

$$\frac{\mathrm{d}\boldsymbol{U}_p}{\mathrm{d}t} = \boldsymbol{F}_D + \boldsymbol{F}_R + \boldsymbol{F}_B + \boldsymbol{F}_S + \frac{g(\rho_p - \rho)}{\rho_p} \tag{9}$$

$\boldsymbol{F_D}$ represents the force acting on the oil droplet caused by velocity difference between gas and oil. The force is proportional to the velocity difference of the two phases and relative Reynolds number (Re_d), given by

$$\boldsymbol{F}_D = 18 \cdot \frac{\mu}{\rho_p D_p^2} \frac{C_D Re}{24} (\boldsymbol{U}_p - \boldsymbol{U}) \tag{10}$$

where D_p is the particle diameter. μ is the molecular viscosity of the fluid. Re_d is the relative Reynolds number, which represents the ratio of inertia force and viscous force. C_D is the viscosity drag coefficient.

$\boldsymbol{F_R}$ is the centrifugal force of unit mass under the rotation coordinate system caused by the rotation of internal field, given by

$$\boldsymbol{F}_R = \frac{U^2}{R} \cdot \mathbf{r} \tag{11}$$

where R represents the distance between the coordinate location of oil droplets and the center axis, and $\boldsymbol{r}$ is the unit vector of R.

In centrifugal separators, the droplet size substantially affects the separation efficiency. For the larger particles, the inertia dominates the motion of particles, which leads the particles to tend to be collected by the inner walls of the separator. While the effect of the inertial forces diminishes as the particle size gets smaller, and the particle response to internal rotation flow shifts to a different regime. For the particles of submicron scale, the Brownian motion and Saffman's lift force dominate the particle motion; therefore, the Brownian motion and Saffman's lift force should be taken into account.

$\boldsymbol{F_B}$ is the Brownian force, and amplitudes of the Brownian force on a sub-micron particle are calculated by the following equations

$$S_{n,ij} = S_0 \delta_{i,j} \tag{12}$$

$$S_0 = \frac{216 \nu k_B T}{\pi^2 \rho D_p^5 \left(\frac{\rho_p}{\rho}\right)^2 C_c} \tag{13}$$

$$F_{bi} = \zeta_i \sqrt{\frac{\pi S_0}{\Delta t}} \tag{14}$$

where $S_{n,ij}$ is the spectral intensity, δ_{ij} is the Kronecker delta function, ν is the kinematic viscosity, T is the absolute temperature of the fluid, C_c is the Cunningham correction factor, and k_B is the Boltzmann constant. F_{Bi} are the amplitudes of the Brownian force components, where ζ_i are zero-mean, unit variance independent Gaussian random numbers.

$\boldsymbol{F_S}$ is the Saffman's lift force of unit mass, which is provided by Saffman[18]

$$F_{si} = \frac{2K\nu^{1/2}\rho d_{ij}}{\rho_p D_p (d_{lk} d_{kl})^{1/4}} (U_i - U_{pi}) \tag{15}$$

where $K = 2.594$ and d_{ij} is the deformation tensor.

Oil droplet evaporation

Oil droplets may evaporate and be converted to stream at high temperature, and once the evaporated oil mixes with air, the mass and momentum exchange of two phases will occur. Here, Berlemont model[15] is adopted to describe oil droplet evaporation, and the dimensionless evaporation rate Λ is defined as

$$\Lambda = \frac{\dot{m}_d C_{vap}}{\pi D_d k} = \frac{2}{Le} \ln(1 + B) \tag{16}$$

where $\dot{m}_d$ is the single droplet mass evaporation rate, C_{vap} is the specific heat of steam, k is the thermal conductivity of the air, Le is Lewis number, which represents the ratio of heat and mass transfer, B is the Spalding number, stands for mass transfer coefficients.

Oil droplet impingement model

Various impingement criterions were put forward on the base of experiments carried out by many scholars.[19,20] The impact weber number is selected as criterion number in this paper, and it varies between 0.1 and 35 by analysis. Combining with Bai's model,[12] impingement phenomena which could happen in the ventilator are mainly adhesion, rebound, and spread, while splash will happen rarely. Therefore, the droplet/wall interaction criteria containing adhesion, rebound and spread are established in this paper, and the solving of rebound selects Bai's model, as shown in Figure 2.

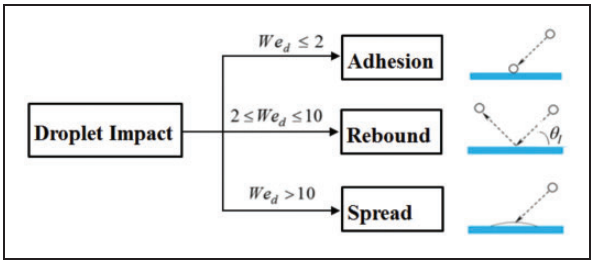

Figure 2. Schematic of droplet–wall interaction criteria.

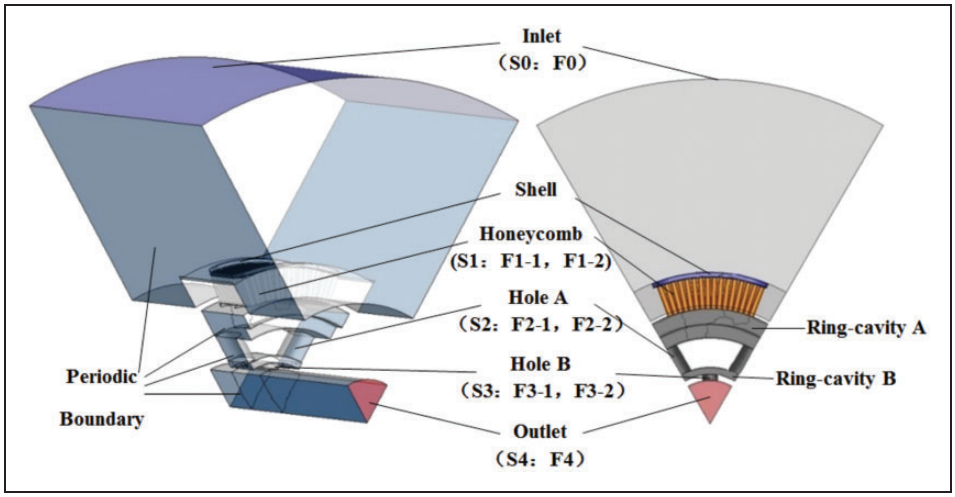

Figure 3. Schematic of axial ventilator with honeycomb.

The impact Weber number (We_d) represents that the ratio of inertia force and surface tension force, defined as

$$We_d = \frac{\rho_d (U_{w,n} - U_{d,n})^2 D_d}{\sigma_d} \quad (17)$$

where, σ_d is the surface tension of oil, $U_{w,n}$ and $U_{d,n}$ refer to the normal component of the wall and the droplet velocity, respectively.

Adhesion phenomenon will occur when the impact weber number of droplets is less than 2, and spread phenomenon will occur when the impact weber number of droplets is more than 10. Considering the oil–gas separation mechanism, adhesion and spread phenomena are both regarded as the oil droplets are completely collected by the wall.

Numerical procedure

Simplified computational domain

Considering the symmetry of axial ventilator with honeycomb, the 1/6 of the whole ventilator structure is selected as the computational domain. Meanwhile, to simulate the external oil–gas environment around the ventilator, the external domain as pressure-stabilizing cavity is added. The size of external domain is related to the external structure of ventilator (bearing chamber, etc.), but cannot affect the internal flow field of the ventilator. It should be noted that the whole domain of ventilator is rotational domain, while the added external domain is stationary domain. Figure 3 shows the computational domain established in this paper, and some related typical cross sections are defined. Si represents the cross-sectional area of inlet, outlet, and radial holes, shown in Table 1, and Fi-1, Fi-2 stand for the inlet and outlet cross section of corresponding radial holes respectively.

Table 1. Cross-sectional area of axial ventilator with honeycomb.

No.	Cross section	Area (mm^2)
1	S0	39,400
2	S1	672
3	S2	260
4	S3	170
5	S4	253

For example, S1 means the middle cross-sectional area of all honeycomb holes, and F1-1, F1-2 are the inlet and outlet cross section of honeycomb structure.

Grids and scheme

Grids are generated by Commercial software GAMBIT. The stationary domain is divided into structural grids, and radial structures of the ventilator (honeycomb hole, Hole A and Hole B) are divided into prism grids with cooper method, whereas ring-cavities and central axis are divided into unstructured grids. The cell numbers of the entire domain are ultimately determined as 2.09 million by checking the grid independence.

The simulations are performed in ANSYS-Fluent version 13.0. The turbulence model selected in this paper is Realizable k–ε, and the near-wall turbulence is solved with two-layer model for enhanced wall treatment (wall spacing of $y^+ < 5$). In addition, for the calculation of the airfield, the finite volume method is adopted to discrete the control equations, and SIMPLE algorithm is adopted to couple the pressure and velocity fields. The pressure discretization employs PRESTO! and momentum, turbulent kinetic energy, and turbulent dissipation rate employ QUICK scheme (second-order accuracy for unstructured grids in this paper).

Table 2. Comparison of numerical results and experimental data.

		ζ		η	
Re_θ ($\times 10^4$)	C_w ($\times 10^4$)	Calculation	Experiment	Calculation (%)	Experiment (%)
3.08	4.74	408.7	423.8	96.47	95.66
8.05	4.74	59.3	61.2	98.54	98.93
12.74	4.74	23.8	24.4	98.65	99.81
12.74	3.56	13.8	14.1	99.12	99.89
12.74	2.37	10.2	11.2	99.36	99.91

Boundary conditions

In order to investigate the performance of axial ventilator well, we select rotation Reynolds number (Re_θ) and nondimensional mass flow rate (C_w) as characteristic variables, defined as follows

$$Re_\theta = \frac{\rho \Omega b^2}{\mu} = 0 \sim 3.22 \times 10^4 \tag{18}$$

$$C_w = \frac{\dot{m}}{\mu b} = (1.096 \sim 5.930) \times 10^4 \tag{19}$$

where represents the rotational speed, and $\dot{m}$ is the air mass flow rate. b is the maximum radius of ventilator structure, and $b = 77$ mm.

The inlet boundary of computational domain is mass flow inlet, and the outlet boundary is pressure outlet. Two sides of computational domain are periodic boundaries, and the remaining are nonslip wall boundaries. After the calculation of airfield is stable, oil droplets enter the computational domain in the middle cross section of external domain, and oil droplet velocity is defined as local air velocity. The oil droplets /wall interaction boundary defined by UDF is set up on the walls of shell, honeycomb holes, ring-cavities, and radial holes, and oil droplet impingement model has been introduced in the previous text.

Results and discussion

Verification of experiment and numerical results

In the study, flow resistance and oil–gas separation efficiency represent the performance of axial ventilator. Here, flow resistance refers to the nondimensional pressure loss, defined as

$$\zeta = \frac{p_{in}^* - p_{out}^*}{\frac{1}{2}\rho \omega^2 b^2} \tag{20}$$

Oil–gas separation efficiency is the ratio of separated oil flux and total oil flux of axial ventilator, expressed as

$$\eta = \frac{Q_{sep}}{Q_{sep} + Q_{non\text{-}sep}} = 1 - \frac{Q_{non\text{-}sep}}{Q_{oil}} \tag{21}$$

where p_{in}^* and p_{out}^* are the inlet and outlet total pressure, respectively. Q_{sep} stands for the separated oil flux by the wall, $Q_{non\text{-}sep}$ is the nonseparated oil flux removed from the outlet, and Q_{oil} means the total oil flux, sum of Q_{sep} and $Q_{non\text{-}sep}$.

The verification for flow resistance and oil–gas separation efficiency between experimental and CFD numerical results is conducted in conditions when environmental temperature is 383 K, rotation Reynolds numbers are $(3.08\text{–}12.74) \times 10^4$, and nondimensional mass flow rates are $(2.37\text{–}4.74) \times 10^4$, as shown in Table 2. It should be noted that the oil droplet diameters are defined as Rossin–Rammler distribution, which is approximate with the experiment environment. The average diameter is 10 μm, the distribution index is 2.7, and the ratio of oil and gas is 2.5%. For the flow resistance, the results have the consistent trend, and the errors of flow resistance in different conditions are all less than 10%, which is in a good agreement. For oil–gas separation efficiency, the numerical results coincide well with the experimental data, and the errors in different conditions are all within 2%, which proves the rationality of numerical model and oil droplets distribution. In summary, the experiment and CFD numerical results verify the reliability of numerical model and results.

Flow field results

The internal flow field of ventilator plays an important role to the motion of oil droplets. Therefore, we first analyze the internal flow field of the typical condition before analyzing the performance of axial ventilator with honeycomb. Figure 4 shows the pressure distributions in the middle cross section of axial ventilator with honeycomb ($Re_\theta = 12.74 \times 10^4$, $C_w = 4.74 \times 10^4$, $T = 373$ K). It can be seen from the figure:

1. The static and total pressure both shows a trend of decreasing in the flow process that the air enters the ventilator from the external domain and leaves from the central axis. The rotation of the ventilator and the decreasing of radial flow area result in the increasing of air velocity, and cause the decreasing of static pressure. In addition, the

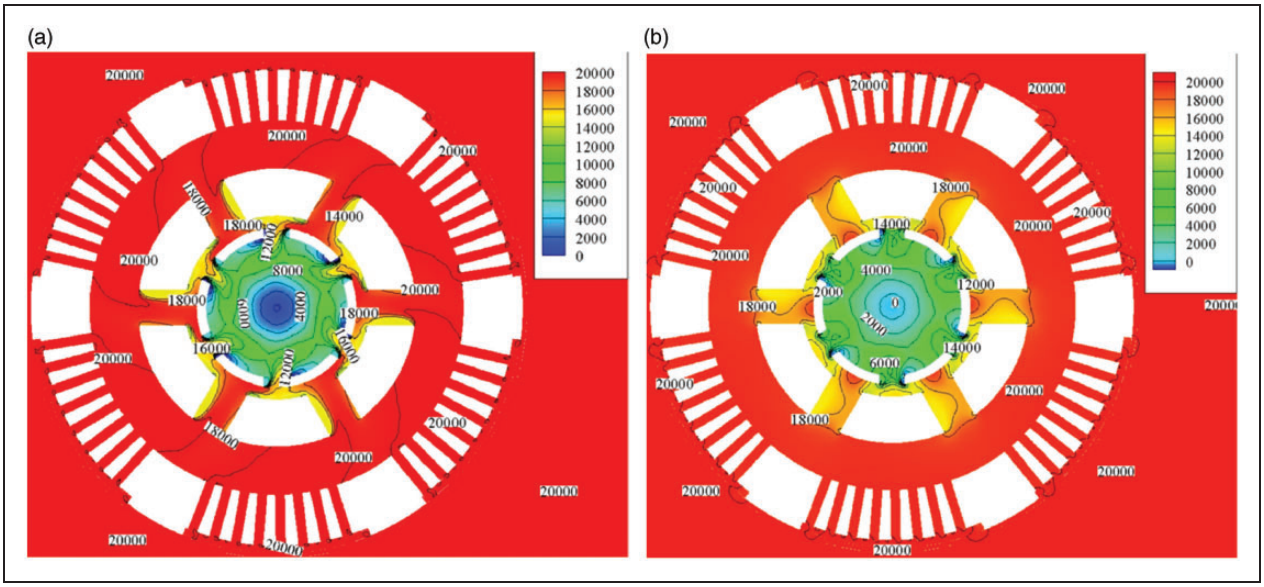

Figure 4. Contours of pressure distribution: (a) total pressure; (b) static pressure.

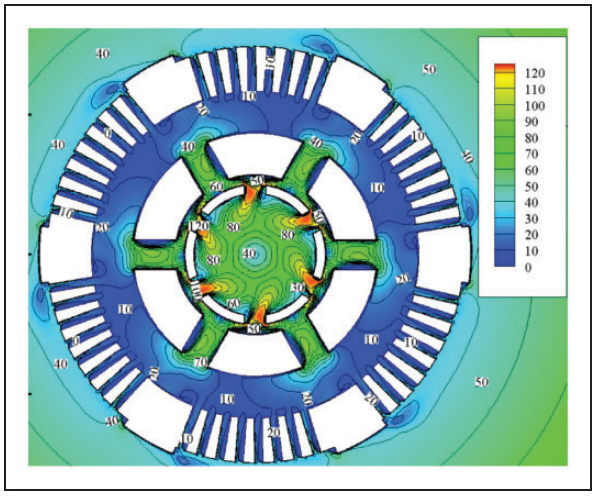

Figure 5. Contours of relative velocity distribution.

complex of ventilator structure and increasing of velocity between air and rotation wall increase the flow loss in the flow process, and decreases the total pressure.

2. For the region of honeycomb structure, static and total pressure both drop little. Combined with the relative velocity contours in Figure 5, the air relative velocity in honeycomb holes changes little within 20 m/s, and is quite lower relative to other regions, which means that flow characteristics of honeycomb holes are good, and the air flow rate in each hole keeps on the same level basically. The main reason is that the cross-sectional area of entire honeycomb holes (S0) is relatively large although a single honeycomb hole is very small, so the air velocity and the flow loss in honeycomb holes keep relatively small. In addition, when the air moves from stationary domain (external domain) to rotational domain, the rotation of ventilator does work to air, which would reduce the total pressure loss.
3. From Hole A to the central axis, the relative velocity of air increases rapidly, and reaches the maximum near the exit of Hole B. Drastic change of air velocity leads to a rapid rise of flow loss, such as in the channel of central axis, the total pressure loss accounts for about 50%, as shown in Table 3. Combined with the cross-sectional area in Table 1, the cross-sectional area decreases rapidly from honeycomb holes to Hole B, nearly 4 times in the area difference, but the cross-sectional area suddenly expands from Hole B to the channel of central axis. Therefore, the sudden contraction and expansion of the cross-sectional area is the main reason of increasing flow loss. In addition, the radial air flows from Hole B, converges in the central axis, forms the vortex, and outflows from the central axis finally, which generates the

Table 3. Flow resistance and proportion of each structure.

Structure	Cross section	Total pressure drop (Pa)	Percentage (%)
External domain	F0→F1-1	−129	−0.79
Honeycomb	F1-1→F1-2	13	0.08
Ring-cavity A	F1-2→F2-1	345	2.14
Hole A	F2-1→F2-2	1280	7.93
Ring-cavity B	F2-2→F3-1	3200	19.83
Hole B	F3-1→F3-2	2732	16.93
Central axis	F3-2→F4	8696	53.88
Whole domain	F0→F4	16,137	100

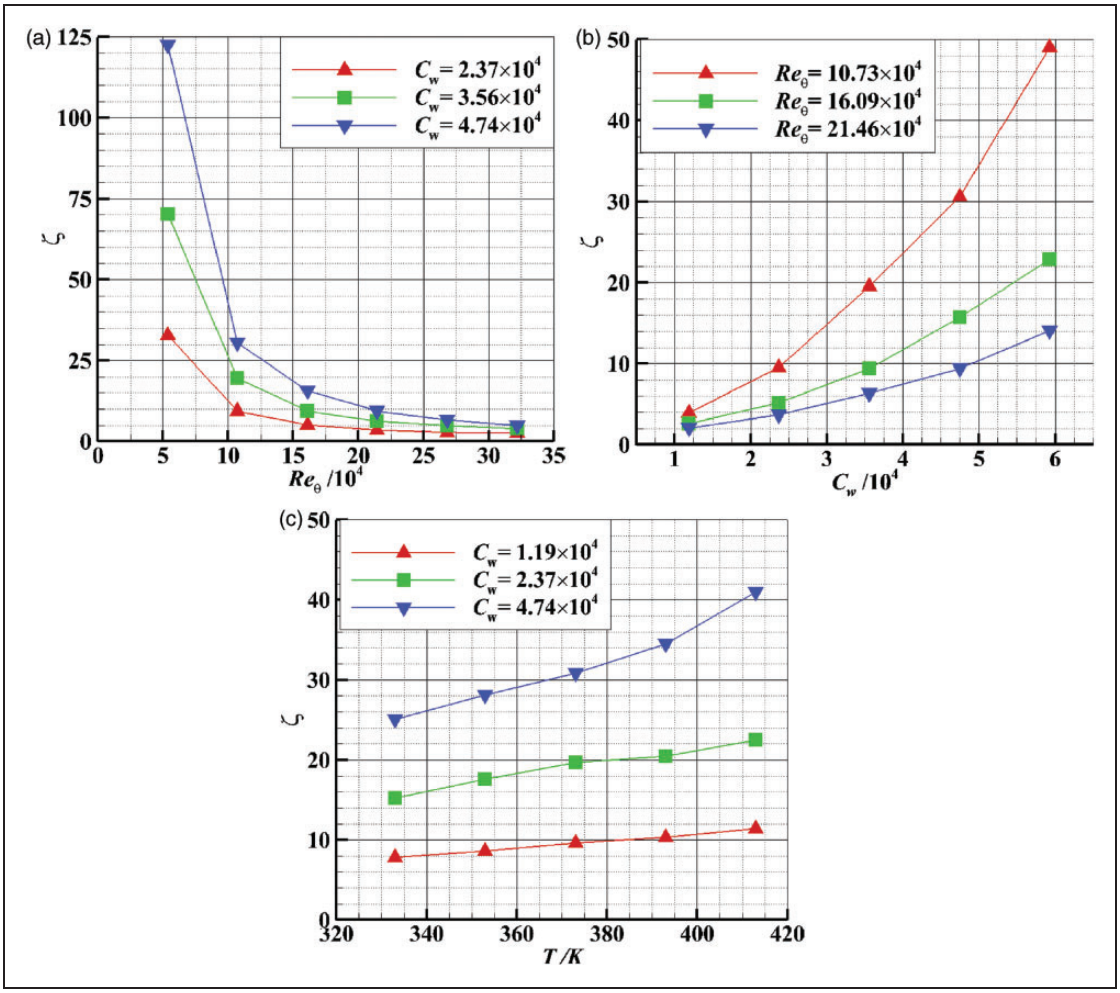

Figure 6. Flow resistance characteristics in different conditions: (a) ζ versus Re_θ with different C_w; ζ versus C_w with different Re_θ; (c) ζ versus T with different C_w.

turbulent dissipation, and results in the increasing of flow resistance also.

Flow resistance characteristics

In order to investigate the flow resistance characteristics of axial ventilator with honeycomb, we obtain the nondimensional pressure loss changes with rotation Reynolds number, nondimensional mass flow rate and environment temperature, as shown in Figure 6.

Figure 6(a) shows the change of nondimensional pressure loss (ζ) versus rotation Reynolds number (Re_θ) with different nondimensional mass flow rates (C_w) at 373 K. The simulated nondimensional pressure loss decreases with the increasing of rotation Reynolds number. As the air moves into the ventilator, the air velocity is generally higher than the velocity of rotation wall, and the velocity difference between them leads to fraction resistance. When rotation Reynolds number is small, the difference is relatively bigger, which will generate a higher resistance; whereas, the fraction resistance will decrease when rotation Reynolds number increases. In addition, the effect of centrifugal pump in the rotation structure also increases the total pressure of air, which will also decrease the nondimensional pressure loss to a certain extent with the increasing of rotation Reynolds number.

Nondimensional pressure loss distribution versus nondimensional mass flow rate at different rotation Reynolds numbers is shown in Figure 6(b), in which the nondimensional pressure loss increases significantly with the increasing of nondimensional mass flow rate. This is mainly because air-circulating velocity increases rapidly with the increasing of nondimensional mass flow rate, which increases the velocity difference between air and rotation wall, resulting in the increasing of flow resistance eventually.

Figure 6(c) presents the distribution of nondimensional pressure loss (ζ) versus environment temperature with different nondimensional mass flow rates ($Re_\theta = 10.73 \times 10^4$). The nondimensional pressure loss increases with the increasing of environment temperature, which is mainly related to the air physical parameters of different environment temperatures. Combined with the air physical parameters as shown in Table 4, the air density will decrease with

the increasing of environment temperatures, which will increase the volume flux in the same mass flow rate, and increases the air circulating velocity. Moreover, the air viscosity will also increase with the increasing of environment temperatures. In short, the increasing of the air circulating velocity and viscosity both increase the flow loss, resulting in the increasing of flow resistance.

Oil–gas separation characteristics

In order to study the oil–gas separation characteristics of axial ventilator with honeycomb, we simulate the oil–gas separation efficiency change with particle diameter, rotation Reynolds number, nondimensional mass flow rate, and environment temperature.

Figure 7 shows the oil–gas separation efficiency distribution with different particle diameters ($C_w = 4.74 \times 10^4$, $T = 373$ K). For different particle diameters, the oil–gas separation efficiency is generally above 80%. When the oil–gas separation efficiency reaches 100%, the particle diameters are all less than 8 μm. Meanwhile, for 5 μm of particle diameter, the oil–gas separation efficiency has reached 100% when $Re_\theta = 32.18 \times 10^4$, and also 99.6% when $Re_\theta = 5.36 \times 10^4$. The filter of honeycomb structure and the rotation of axial ventilator are the main reasons of relatively high oil–gas separation efficiency. Furthermore, the oil–gas separation efficiency increases with the increasing of rotation Reynolds number for the increasing of the drag force and centrifugal force generally, but when the particle diameter is less than 1 μm, the magnitude of particle diameter can also affect the variation of oil–gas separation efficiency locally. For instance, between 0.6 and 0.8μm, the oil–gas separation efficiency of $Re_\theta = 21.46 \times 10^4$ is larger than that of $Re_\theta = 32.18 \times 10^4$. This is because when the particle diameter varies near the scale of submicron (less than 1 μm), the effective forces (Brownian and Saffman) will become more and more significant to the motion of the oil droplets, which affect the oil–gas separation efficiency for a certain extent.

Figure 8(a) shows the distribution of oil–gas separation efficiency (η) versus rotation Reynolds number (Re_θ) with different particle diameters ($C_w = 4.74 \times 10^4$, $T = 373$ K). When $Re_\theta = 0$, the oil–gas separation efficiencies are the lowest for different particle diameters, while once the axis ventilator rotates, the oil–gas separation efficiency increases rapidly. After that, the growth rate of oil–gas separation efficiency becomes relatively slow. It is known that the honeycomb structure has large contact area, which is advantageous to the collection of the oil droplets, but honeycomb holes are all radial, which mean that the advantage will not be taken if the ventilator does not rotate. Moreover, the centrifugal force of oil droplets increases with the increasing of rotation Reynolds number, which increases the velocity difference between air and oil, so in the same residence time, more oil droplets will be thrown to the wall and

Table 4. Air physical parameters.

Temperature (K)	333	353	373	393	413
Density (kg/m^3)	1.06	1.0	0.946	0.898	0.854
Dynamic viscosity (10^{-5}kg/(ms))	2.01	2.11	2.19	2.28	2.37

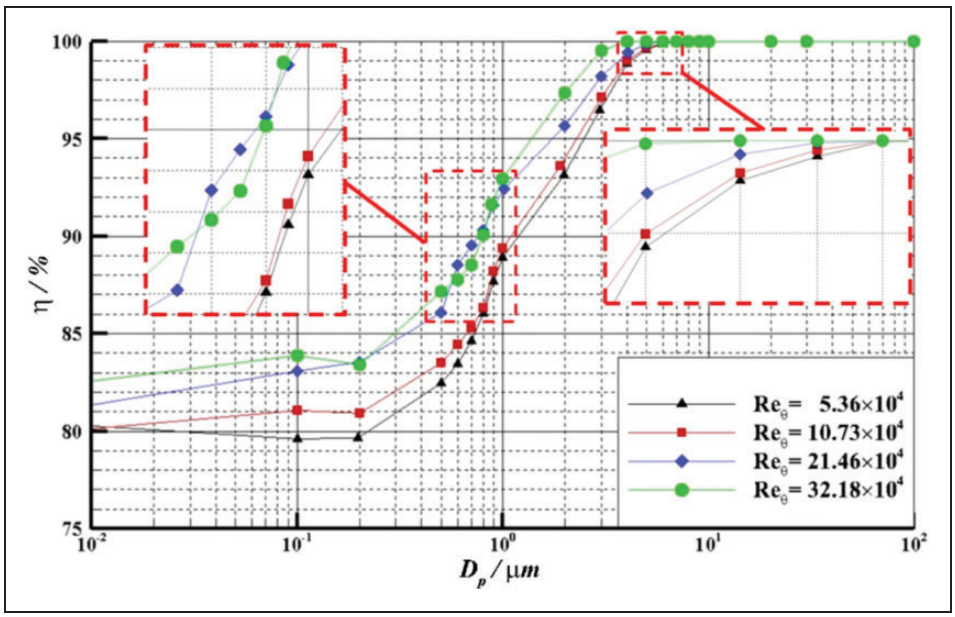

Figure 7. Effect of particle diameters on separation efficiency.

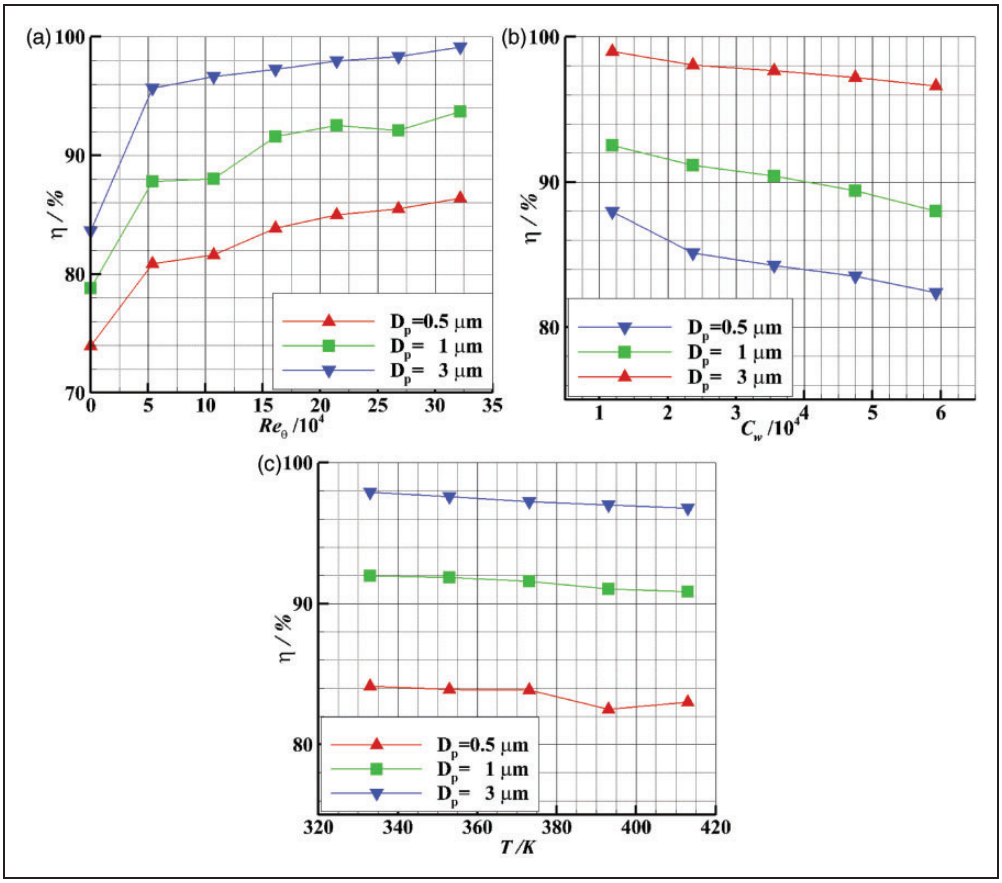

Figure 8. Oil–gas separation characteristic in different conditions: (a) η versus Re_θ; (b) η versus C_w; (c) η versus T.

collected under the action of inertial force, which results in the increasing of oil–gas separation efficiency.

Figure 8(b) presents the change of oil–gas separation efficiency (η) versus nondimensional mass flow rate (C_w) with different particle diameters ($Re_\theta = 10.73 \times 10^4$, $T = 373$ K). The simulated oil–gas separation efficiency decreases with the increasing of C_w. The oil droplet circulating velocity increases with the increasing of C_w, which will cause two effects below: one is the increasing of the shear force (drag force) to oil droplets, which will enhance the ability that oil droplets overcome the inertia force and the centrifugal force. The other is the decreasing of the residence time that the oil droplets stay in the ventilator. Hence, more oil droplets will eventually escape from the ventilator based on the above effects, and the oil–gas separation efficiency decreases with the increasing of C_w.

The oil–gas separation efficiency (η) distribution versus environment temperature with different particle diameters ($Re_\theta = 16.09 \times 10^4$, $C_w = 4.74 \times 10^4$) is presented in Figure 9(c), in which the oil–gas separation efficiency decreases slightly with the increasing of environment temperature. As mentioned above, the air density decreases with the increasing of environment temperature, results in the increasing of the air circulating velocity. Just as the separation efficiency distribution with nondimensional mass flow rate, the separation efficiency decreases with the increasing of environment temperature. However, compared with rotation Reynolds number and nondimensional mass flow rate, the effect of environment temperature is relatively small.

Contribution efficiency of honeycomb structure

The ventilator shell, honeycomb structure, ring-cavities, and radial holes can all collect the oil droplets. In order to investigate the oil–gas separation ability of honeycomb structure further, we obtain and analyze the effect of the honeycomb structure to oil–gas separation. In this paper, the local separation contribution efficiency (α) is introduced, which refers to the ratio of separated oil flux in the local structure and separated oil flux of axial ventilator, expressed as

$$\alpha = \frac{Q_{in} - Q_{out}}{Q_{sep}} \tag{22}$$

where Q_{in} and Q_{out} stand for the inlet and outlet oil flux of local structure, respectively.

Figure 9(a) shows the distribution of oil–gas separation contribution efficiency (α) of honeycomb structure versus rotation Reynolds number (Re_θ) with different particle diameters ($C_w = 4.74 \times 10^4$,

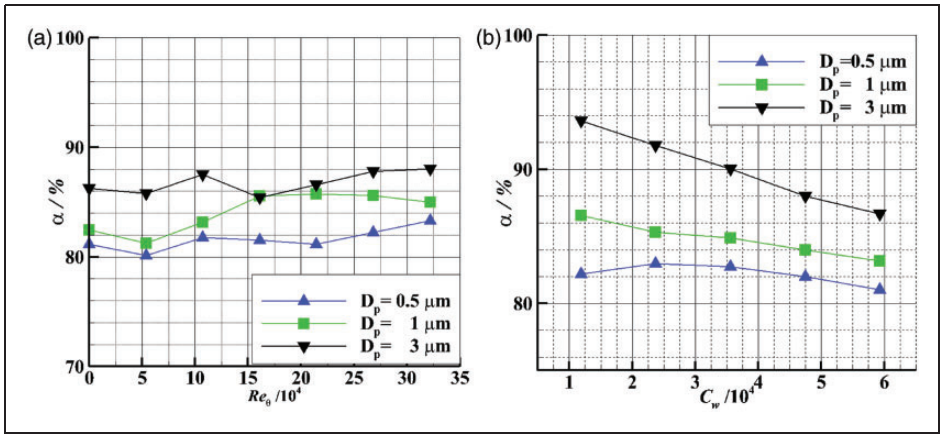

Figure 9. Separation contribution efficiency of honeycomb structure: (a) α versus Re_θ; (b) α versus C_w.

$T = 373$ K). The oil–gas separation contribution efficiency of honeycomb structure fluctuates slightly with different Re_θ, but is generally more than 80%, which indicates that the separated oil in the honeycomb structure accounts for the vast majority of total separated oil in the ventilator. Moreover, although the oil–gas separation efficiency increases with the increasing of Re_θ, the proportion of the separated oil in the honeycomb structure keeps unchanged in the main, which means that the contribution efficiency is not sensitive for Re_θ.

Figure 9(b) presents the change of oil–gas separation contribution efficiency (α) of honeycomb structure versus nondimensional mass flow rate (C_w) with different particle diameters ($Re_\theta = 10.73 \times 10^4$, $T = 373$ K). The oil–gas separation contribution efficiency of honeycomb structure shows the trend of decreasing with the increasing of C_w, and the larger the particle diameter, the more obvious the decreasing. The increasing of C_w increases the air circulating velocity, and reduces the residence time of the oil droplets in the honeycomb structure, so when the mixture of oil and air leaves the honeycomb structure, the oil concentration remains relatively higher, which increases the amount of oil separation in ring-cavities and holes, and decreases the contribution efficiency of the honeycomb structure.

Conclusions

In the present study, the reasonable oil /air two-way coupling model and droplet impact model is proposed, and the performance of axial ventilator with honeycomb is obtained. The main conclusions are threefold:

(a) The axial ventilator with honeycomb designed here has favorable separation efficiency, which is estimated as 99.6% for an average oil droplet diameter of 5 μm, and able to collect 100% of the oil particles when the diameter is larger than 8 μm. Furthermore, the honeycomb structure plays a major role in the oil–gas separation of axis ventilator where the amounts of separated oil account for 80% at least.

(b) The nondimensional pressure loss increases with the increasing of nondimensional mass flow rate and environment temperature, but the decreasing of rotation Reynolds number. The flow resistance mainly produced in the channel of central axis, and the flow resistance in the honeycomb structure is relatively low by contract.

(c) The increasing of rotation Reynolds number leads to the increasing of separation efficiency by enhancing centrifugal force. The increasing of nondimensional mass flow rate and environmental temperature boost the circulating velocity of air, which not only reduces the residence time of oil droplets in the axial ventilator, but also enhances the ability of overcoming inertial forces and centrifugal forces for the oil droplets, resulting in the decreasing of separation efficiency.

Declaration of Conflicting Interests

The author(s) declared no potential conflicts of interest with respect to the research, authorship, and/or publication of this article.

Funding

The author(s) disclosed receipt of the following financial support for the research, authorship, and/or publication of this article: The work has been supported by the Project Supported by Natural Science Basic Research Plan in Shaanxi Province of China, contact 2015JQ5194, and the Fundamental Research Funds for the Central Universities, contact 3102015ZY090.

References

1. Lin JH. *Design of mechanical system of aero gas turbine engine*. Beijing: Aviation Industry Press, 2005, pp.74–77.
2. Elsayed K and Lacory C. Modeling and optimization of the cyclone separator application of response surface methodology for minimum pressure drop. In: *5th European conference on computational fluid dynamics*, Lisbon, Portugal, 14–17 June 2010, pp.14–17.

3. Eastwick CN, Simmons K, Wang Y, et al. Study of aero-engine oil–air separators. *Proc J Power and Energy* 2006; 220: 707–717.
4. Xu R, Zong Q, Liu L, et al. Effect of turbulent dispersion on oil/gas separation process in axial ventilator. *Aeroengine* 2011; 37(4): 5–9.
5. Farrall M. *Numerical modeling of two-phase flow in a simplified bearing chamber*. Nottingham: University of Nottingham, 2000.
6. Bachalo DW. Measurement techniques for turbulent two-phase flow research. *International symposium on multiphase fluid, non-Newtonian fluid and physicochemical fluid flows*. Beijing, China, 1997.
7. Gorse P, Busam S and Dullenkopf K. Influence of operating condition and geometry on the oil film thickness in aeroengine bearing chamber. *J Eng Gas Turb Power* 2006; 128: 103–110.
8. Lu YG, Zhang MH, Liu ZX, et al. Numerical study and validation for two-phase flow of oil and gas in aeroengine bearing chambers. *J Aerosp Power* 2014; 29: 2751–2757.
9. Zhao JY, Liu ZX, Hu JP, et al. Motion of wall oil film with consideration of oil-gas coupled heat and mass transfer in the bearing chamber. *J Propul Technol* 2014; 35: 973–980.
10. Mundo C, Sommerfeld M and Tropea C. Droplet-wall collisions: Experimental studies of the deformation and breakup process. *Int J Multiphase Flow* 1995; 21: 151–173.
11. Cossali GE, Coghe A and Marengo M. The impact of a single drop on a wetted solid surface. *Exp Fluids* 1997; 22: 463–472.
12. Bai CX and Gosman AD. Development of methodology for spray impingement simulation. In: *International congress and exposition*, SAE Technical Paper No. 950283, 1995.
13. Stanton D and Rutland C. Modeling fuel film formation and wall interaction in diesel engines. In: *International congress and exposition*, SAE Technical Paper No. 960628, 1996.
14. Willenborg K, Klingsporn M, Tebby S, et al. Experimental analysis of air/oil separator performance. *J Eng Gas Turb Power* 2008; 130: 1495–1506.
15. Berlemont A, Grancher M and Gouesbet G. Heat and mass transfer coupling between vaporizing droplets and turbulence using a Lagrangian approach. *Int J Heat Mass Transfer* 1994; 38: 3023–3034.
16. William BW and Mark GP. Semi-empirical modeling of SLD physics. In: *Proceedings of 42nd AIAA aerospace sciences meeting and exhibit*, paper no. AIAA-2004-0412, Reno, Nevada, America, 2004.
17. Liu DY. *Fluid dynamics of two-phase systems*. Beijing: Higher Education Press, 1993, pp.26–33.
18. ANSYS Inc. *ANSYS fluent 13.0 User's Guide*. New Hampshire: ANSYS Inc, 2011.
19. Trujilloy MF, Mathews WS, Lee CF, et al. Modeling and experiment of impingement and atomization of a liquid spray on a wall. *Int J Engine Res* 2000; 1: 87–105.
20. Mundo C, Tropea C and Sommerfeld M. Numerical and experimental investigation of spray characteristics in the vicinity of a rigid wall. *Exp Therm Fluid Sci* 1997; 15: 228–237.

Appendix

Notation

B	Spalding number
C_c	Cunningham correction factor
C_D	viscosity drag coefficient
C_{vap}	evaporation specific heat
C_w	nondimensional mass flow rate
d_{ij}	deformation tensor
E	internal energy and mean
$\boldsymbol{F}$	force of unit mass
k	thermal conductivity
Le	Lewis number
M	molecular viscosity of the fluid
p^*	total pressure
Q	oil flux
q_s	heat rate on droplet surface
Re	relative Reynolds number; rotation Reynolds number
S	additional source term
$S_{n,ij}$	spectral intensity
T	temperature
U	gas velocity
We_d	impact Weber number
α	local separation contribution efficiency
δ_{ij}	Kronecker delta function
η	oil–gas separation efficiency
Ω	rotational speed
ρ	gas density
τ	shear stress
ν	kinematic viscosity
ζ	nondimensional pressure loss
Λ	dimensionless evaporation rate

Subscript

d	droplet
E	energy source
m	continuity source
U	momentum source
in	inlet
out	outlet